frontiers | Frontiers in Chemistry

TYPE Original Research
PUBLISHED 10 October 2022
DOI 10.3389/fchem.2022.1027713

OPEN ACCESS

EDITED BY
Tao Wei,
Jiangsu University of Science and Technology, China

REVIEWED BY
Tian Xia,
Heilongjiang University, China
Shuiyun Shen,
Shanghai Jiao Tong University, China
Xiaoliang Zhou,
Southwest Petroleum University, China

*CORRESPONDENCE
Qun Yi,
yq202109@wit.edu.cn
Wang Sun,
sunwang@bit.edu.cn

SPECIALTY SECTION
This article was submitted to Electrochemistry, a section of the journal Frontiers in Chemistry

RECEIVED 25 August 2022
ACCEPTED 21 September 2022
PUBLISHED 10 October 2022

CITATION
Zhen S, Zhang L, Xu C, Zhang D, Yi Q, Sun W and Sun K (2022), Ti/Ni co-doped perovskite cathode with excellent catalytic activity and CO_2 chemisorption ability via nanocatalysts exsolution for solid oxide electrolysis cell.
Front. Chem. 10:1027713.
doi: 10.3389/fchem.2022.1027713

Ti/Ni co-doped perovskite cathode with excellent catalytic activity and CO_2 chemisorption ability *via* nanocatalysts exsolution for solid oxide electrolysis cell

Shuying Zhen[1], Lihong Zhang[2], Chunming Xu[2], Ding Zhang[3], Qun Yi[3]*, Wang Sun[2]* and Kening Sun[2]

[1]State Key Laboratory for Advanced Metals and Materials, University of Science and Technology Beijing, Beijing, China, [2]Beijing Key Laboratory for Chemical Power Source and Green Catalysis, Beijing Institute of Technology, Beijing, China, [3]School of Chemical Engineering and Pharmacy, Wuhan Institute of Technology, Wuhan, China

Carbon dioxide (CO_2) gas is the main cause of global warming and has a significant effect on both climate change and human health. In this study, Ni/Ti co-doped $Sr_{1.95}Fe_{1.2}Ni_{0.1}Ti_{0.2}Mo_{0.5}O_{6-\delta}$ (SFNTM) double perovskite oxides were prepared and used as solid oxide electrolysis cell (SOEC) cathode materials for effective CO_2 reduction. Ti-doping enhances the structural stability of the cathode material and increases the oxygen vacancy concentration. After treatment in 10% H_2/Ar at 800°C, Ni nanoparticles were exsolved *in situ* on the SFNTM surface (Ni@SFNTM), thereby improving its chemisorption and activation capacity for CO_2. Modified by the Ti-doping and the *in situ* exsolved Ni nanoparticles, the single cell with Ni@SFNMT cathode exhibits improved catalytic activity for CO_2 reduction, exhibiting a current density of 2.54 A cm^{-2} at 1.8 V and 800°C. Furthermore, the single cell shows excellent stability after 100 h at 1.4 V, indicating that Ni/Ti co-doping is an effective strategy for designing novel cathode material with high electrochemical performance for SOEC.

KEYWORDS

solid oxide electrolysis cells (SOECs), double perovskite oxide, cathode, *in situ* exsolution, CO_2 reduction reaction

Introduction

Carbon dioxide (CO_2), a greenhouse gas and the main cause of global warming, has a significant impact on both climate change and human health. (Armaroli and Balzani, 2011; Broecker, 2018; Hoegh-Guldberg et al., 2019). The capture and utilization of CO_2 is a promising approach to effectively reduce CO_2 concentration and emissions (Fu et al., 2019; Karanikolos et al., 2021). It is known that CO can be further converted to low-

carbon fuels and high value added chemicals through subsequent Fischer-Tropsch reactions (Zhang et al., 2002; Quadrelli et al., 2011). Therefore, converting CO_2 to CO is a feasible and important method for CO_2 utilization. Solid oxide electrolysis cells (SOEC) are high-efficiency electrochemical reactors that can convert CO_2 into CO using distributed renewable energy, with an efficiency close to 100 % (Singh et al., 2015; Li et al., 2021). Normally, the CO_2 reduction reaction (CO_2-RR) occurs at the cathode of the SOEC, where CO_2 is electrochemically converted to CO and oxygen ions under an applied potential. The generated oxygen ions are transferred across the solid electrolyte to the anode and converted to O_2. The cathode is the core component in the SOEC, and dominates the electrochemical CO_2-RR process and the performance of the SOEC.

Presently, Ni-YSZ is the most widely used cathode in SOEC for CO_2-RR, owing to its good electrocatalytic activity and cost effectiveness (Song et al., 2018; Xu et al., 2019). However, certain inevitable issues hinder its further application, including Ni oxidation during the CO_2/CO redox reaction process in the absence of a safe gas (H_2/CO), carbon deposition at high CO concentrations, and Ni particle growth during long-term operation (Dong et al., 2017; Sciazko et al., 2021; Yang et al., 2022). Materials comprising perovskite oxide with mixed ionic-electronic conductivity, such as $Sr_2Fe_{1.5}Mo_{0.5}O_{6-\delta}$ (SFM), show promise for SOEC, and exhibit excellent redox stability, coke resistance, and long-term stability (Li et al., 2017a; Zhang et al., 2021). Nevertheless, compared with the Ni-YSZ cathode material, SFM oxide exhibits weak chemical CO_2 adsorption and inadequate catalytic activity for CO_2-RR, which limits the performance of CO_2 electrolysis. Recently, the *in situ* exsolution of transition metal nanoparticles on the surface of perovskite oxide substrates has attracted extensive research attention and is regarded as a promising strategy to enhance the electrocatalytic activity of perovskite oxides. (Wang et al., 2019; Xu et al., 2021)

Briefly, the exsolved metal nanocatalysts, uniformly dispersed on the surface, can effectively strengthen the adsorption capacity of CO_2 and improve the electrolysis activity for CO_2-RR. Abundant oxygen vacancies were created during the reduction process, thereby supplying more active reaction regions for the chemisorption and catalytic activation of CO_2 molecules on the electrode surface (Liu S. B. et al., 2016; Zheng et al., 2017). Furthermore, the metal nanoparticles were firmly anchored on the surface of the electrode material, restricting their aggregation. The strong interaction of the metal-oxide interface also exhibits exceptional electrocatalytic activity for the CO_2-RR. Chen et al. concluded that exsolved NiFe alloy nanoparticles in $Sr_{1.9}Fe_{1.5}Mo_{0.4}Ni_{0.1}O_{6-\delta}$ enhanced the chemisorption capacity and reaction kinetics of CO_2 on the cathode surface (Wang et al., 2016). Bao et al. demonstrated that *in situ* exsolved $FeNi_3$ nanoparticles on the $Sr_2Fe_{1.35}Mo_{0.45}Ni_{0.2}O6_{-\delta}$ material strengthened CO_2 adsorption and facilitated subsequent CO_2-RR in SOEC (Lv et al., 2019). Luo et al. confirmed that *in situ* exsolved Fe-Ni nanospheres are evenly anchored on the perovskite oxide with oxygen defects, greatly enhancing the catalytic performance of the material as a highly stable and efficient catalyst (Liu S. et al., 2016). However, SFM-based double perovskite oxides tend to transform into Ruddlesden-Popper (RP)-type layer perovskite oxides during the *in situ* exsolution process in the reduction treatment, causing the initial perovskite structure to deform (Park et al., 2019; Park et al., 2020; Choi et al., 2021). The structural stability can be enhanced by employing stable valence state metallic elements, such as Ti^{4+}, Zr^{4+}, and Nb^{5+} in severe reducing atmospheres. For example, we introduced a stable valence Ti element to the B-site of SFM oxide, which notably improved its structural stability, produced abundant oxygen vacancies and increased the conductivity of the oxygen ions (Xu et al., 2022).

Herein, a Ti and Ni co-doped double perovskite oxide ($Sr_{1.95}Fe_{1.2}Ni_{0.1}Ti_{0.2}Mo_{0.5}O_{6-\delta}$, SFNTM) was synthesized. After the reduction treatment, the oxide matrix maintained the original perovskite structure, while *in situ* exsolved Ni nanoparticles were uniformly anchored on its surface to form a metal-oxide heterostructure (Ni@SFNTM) as SOEC cathodes for CO_2-RR at high temperatures. Subsequently, the phase structure, CO_2 chemisorption and activation, and electrochemical properties of SFNTM and Ni@SFNTM samples were studied. The heterostructure formed by the *in situ* exsolved Ni nanoparticles and the SFNTM matrix can enhance the CO_2 adsorption activity and expand the abundant CO_2-RR active sites, thus further enhancing its performance.

Experimental section

Material preparation and cell fabrication

An $Sr_{1.95}Fe_{1.2}Ni_{0.1}Ti_{0.2}Mo_{0.5}O_{6-\delta}$ (SFNTM) sample was prepared using a modified sol-gel combustion method. The calculated stoichiometric ratios of $Ni(NO_3)_2{\cdot}6H_2O$, $Sr(NO_3)_2$, $Fe(NO_3)_3{\cdot}9H_2O$, and $(NH_4)_6Mo_7O_{24}{\cdot}4H_2O$ were added to deionized water and stirred at 80°C. $C_{16}H_{36}O_4Ti$ was dissolved in ethanol, and the content was added dropwise into the abovementioned solution. Subsequently, citric acid and glycine were added, and a gel was obtained *via* continuous mixing. A black precursor powder was obtained by heating the gel at 250°C followed by sintering at 1,100°C for 5 h to synthesize SFNMT oxide. The $La_{0.6}Sr_{0.4}Co_{0.2}Fe_{0.8}O_3$ (LSCF) cathode, $Ce_{0.8}Sm_{0.2}O_2$ (SDC), and $La_{0.8}Sr_{0.2}Ga_{0.8}Mg_{0.2}O_3$ (LSGM) electrolyte materials were purchased from Fuel Cell Co. The Ni@SFNTM sample was prepared by reducing the SFNTM in 5 % H_2/Ar at 800°C for 5 h.

An electrolyte-supported single cell (SFNTM/Ni@SFNTM|SDC|LSGM|LSCF) was used. Dense disk-shaped LSGM electrolyte flakes (~300 μm) were formed by dry-pressing and calcined at 1,450°C for 6 h. The SDC slurry was formulated by mixing SDC powder and a binder comprising a mixture of ethyl

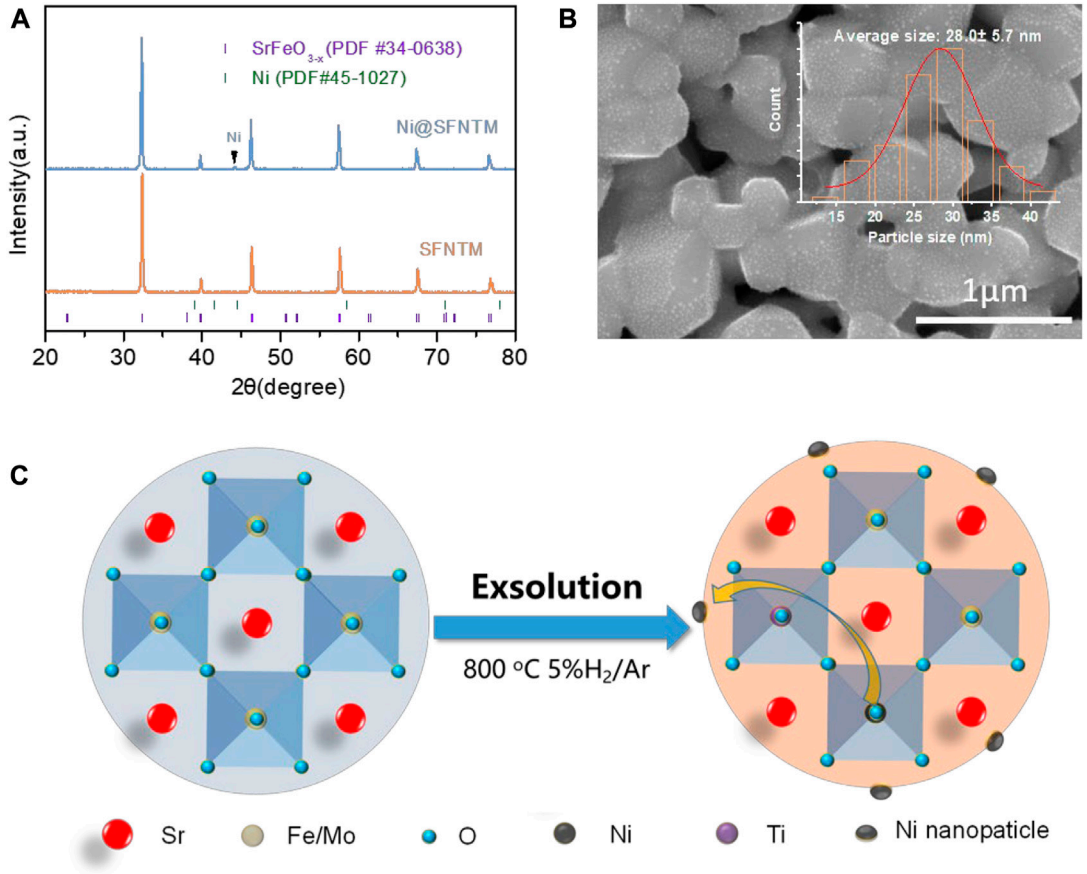

FIGURE 1
(A) XRD patterns of SFTM and Ni@SFNTM powders, **(B)** SEM image of Ni@SFNTM, inset is particle size distribution of Ni nanoparticles, **(C)** Schematic diagram of *in situ* exsolution of SFNTM under reducing conditions.

cellulose and α-terpineol, which was screen-printed onto the two sides of the LSGM electrolyte pellet and subsequently calcined at 1,350°C for 3 h. The LSCF and SFNTM/SFTM ink were formulated by combining the LSCF and SFNTM/SFTM powders with a binder. The LSCF anode and SFNTM/SFTM cathode ink were symmetrically screen-printed onto both sides of the electrolyte pellet and calcined at 1,100°C for 2 h. Silver ink and silver wires were used to cover the electrode surface and the electrode was fired at 750°C for 1 h to act as the current collector.

Characterization

The crystal structures of the as-synthesized and reduced SFNTM samples were investigated using X-ray diffraction (XRD, X'Pert Pro MPD diffractometer). The morphologies and microstructures of the reduced samples were observed using field-emission transmission electron microscopy (FETEM, JEM-2010F) and Scanning electron microscopy (SEM, FEI QUANTA-250). XPS (MULT1LAB 2000) was conducted to characterize the surface valence compositions of the different elements. Temperature-programmed desorption of CO_2 (CO_2-TPD) measurements were performed using a Micromeritics 2000 instrument with an Ar carrier gas, and the temperature was increased from 50°C to 1,000°C at a rate of 10°C min^{-1}. The prepared materials were first treated under a He atmosphere at 300°C. The oxygen vacancy defects were detected by EPR (Bruker ELEXSYS E500). EPR tests were performed at 600 K with 10 mg sample and the sweep width is 1000G. The synthesized samples were tested by a four-probe direct current method. The Keithley 2,400 source meter was used to test on the dense bar shapes with a size of 2 mm × 4 mm×10 mm, which were prepared by dry pressing method and subsequently sintered at 1,200°C for 3 h, resulting in a density of over 95%. Electrical conductivity relaxation (ECR) measurement were performed under an abrupt switch of the atmosphere from 2:1 CO–CO_2 to 1:1 CO–CO_2. The variations in conductivity and test time were carried out until new equilibrium conditions are finally reached. Electrochemical impedance spectroscopy (EIS) of a single cell was performed using an

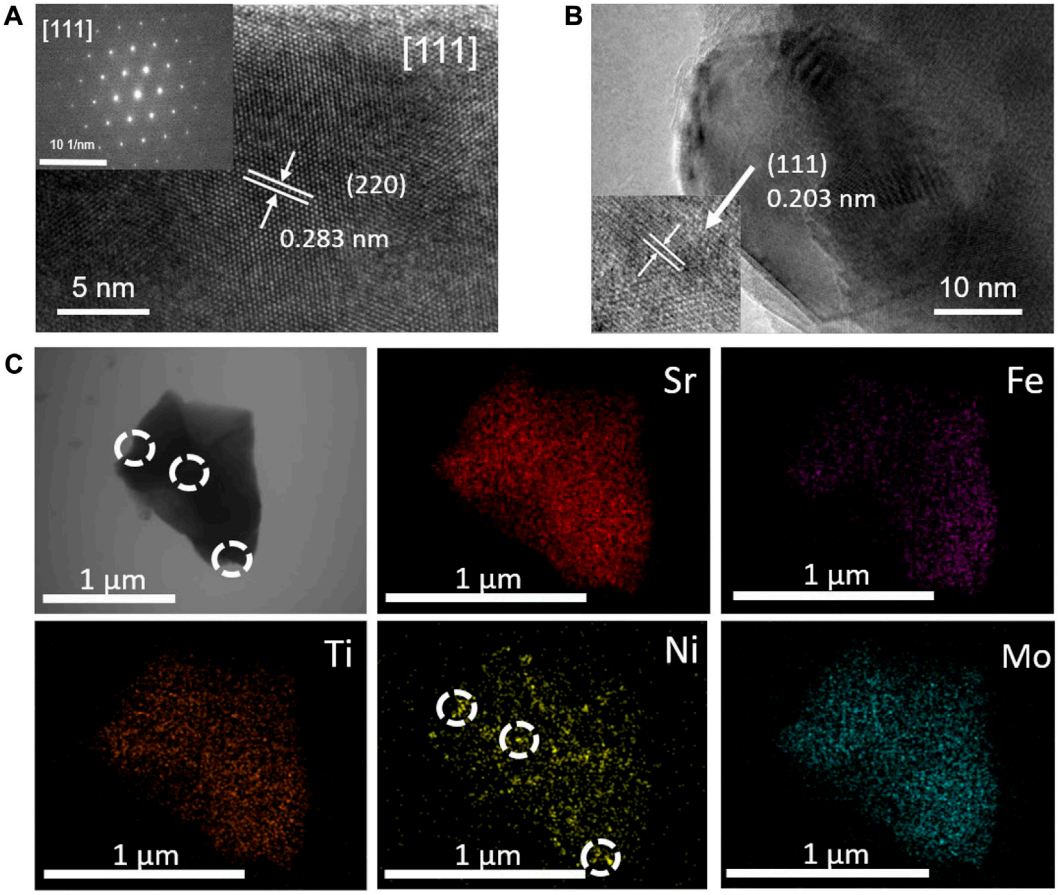

FIGURE 2
(A) HRTEM images and corresponding SEAD image patterns of SFNTM substrate; **(B)** HRTEM images of Ni nanoparticles; **(C)** STEM image and corresponding EDS maps of Ni@SFNTM

AutoLab 302N at an open circuit voltage (OCV) by passing pure CO_2 gas into the cathode at a flow rate of 50 ml min^{-1} while directly exposing the anode side to ambient gas. The corresponding AC impedance was analyzed using ZSimpWin software. The composition of the exhaust gas was evaluated using the online gas chromatography.

Results and discussion

Material structural characterization

XRD was used to characterize the crystal structures of the SFNTM and Ni@SFNTM samples at room temperature. Figure 1A shows the XRD pattern of the SFNTM sample after calcination at 1,100°C for 5 h and the XRD pattern of the Ni@SFNTM sample after reducing SFNTM in 5% H_2/Ar at 800°C for 5 h. The SFNTM sample presents a pure cubic perovskite structure, which is consistent with that of the PDF card (PDF #34–0638) with no impurity phase; this result confirms that Ti and Ni were successfully co-doped into the perovskite structure. It should be noted that Ni@SFNTM maintains the cubic perovskite structure after the reducing treatment, which is consistent with the Rietveld refinement data (Supplementary Figure S1 and Supplementary Table S1). At the same time, there is an obvious Ni element peak in the XRD pattern of the Ni@SFNTM sample, which is consistent with that of the PDF card (PDF #34–0638), indicating that Ni can be exsolved *in-situ* from the SFNTM matrix under reducing conditions. Furthermore, the (110) peak of Ni@SFNTM shifts to a reduced angle, showing lattice expansion that results from the reduction of the B-site transition metal and the generation of oxygen vacancies. A small peak corresponding to Ni metal is observed for the Ni@SFNTM sample, showing that Ni can be exsolved *in situ* from the SFNTM matrix (Figure 1C). SEM analysis was used to observe the microstructures of the SFNTM and Ni@SFNTM particles. Figure 1B and Supplementary Figure S2 show that the SFNTM particles are

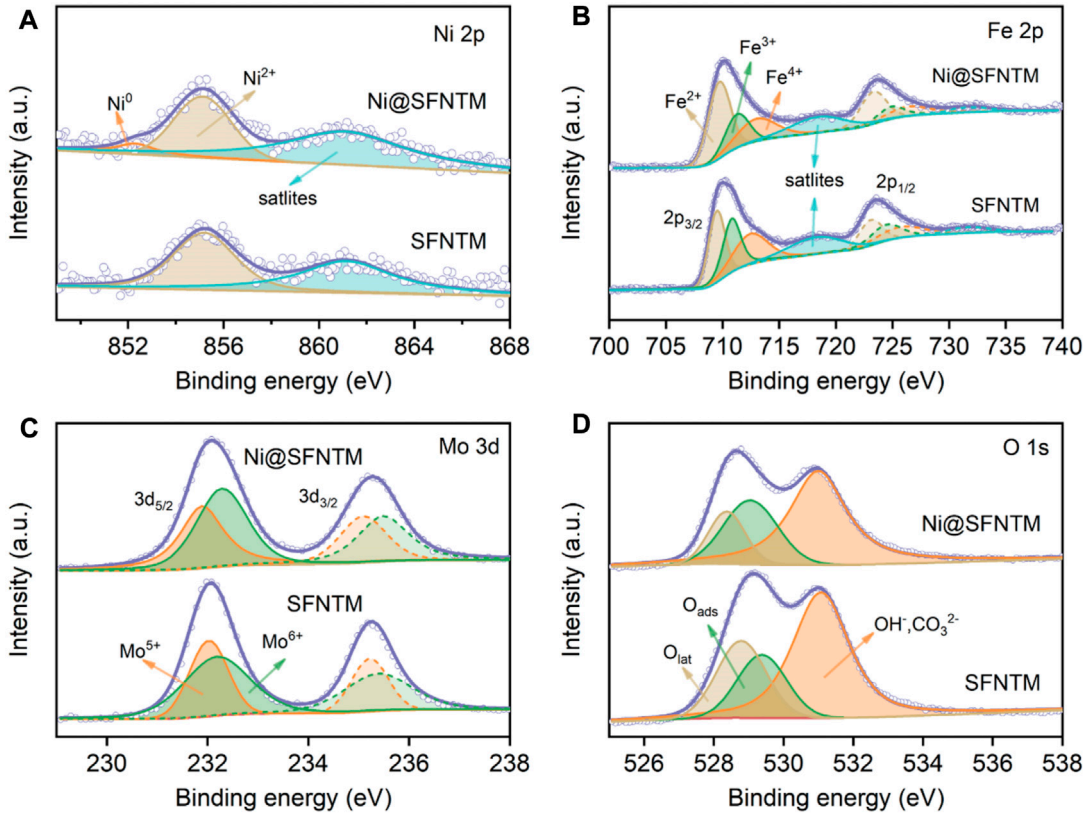

FIGURE 3
XPS characterization of SFNTM and Ni@SFNTM samples: **(A)** Ni 2p spectra, **(B)** Fe 2p spectra, **(C)** Mo 3 d spectra, **(D)** O 1s spectra.

interconnected with a smooth surface. After the reduction treatment, Ni@SFNTM presents a glossy surface, while spherical Ni nanoparticles with a mean size of 28 nm are uniformly distributed on the surface of the SFNTM perovskite substrate.

To further explore the composition and crystal structure of the synthesized samples, HRTEM characterization was performed on the Ni@SFNTM powder. As shown in Figure 2A, the SAED pattern comprises an image of the particles along the (111) crystal axis, which further confirms that the crystal structure of the SFNTM substrate is a cubic perovskite with a spatial group of Fm-3m. The observed lattice fringe distance of 0.283 nm corresponds to the (220) facet of the cubic SFNTM perovskite, which agrees with the XRD data. Moreover, as shown in Figure 2B, the interplanar spacing (0.203 nm) of the nanoparticles is assigned to the (111) plane of the Ni metal. The spherical Ni nanoparticles are partially anchored in the SFNTM substrate, suggesting extended catalytic active sites and strong bonding between the nanoparticles and the substrate, which greatly enhances the chemical and thermal stability. EDS mapping was performed to further determine the elemental composition of the Ni@SFNTM (Figure 2C). All the elements in the SFNTM substrate are evenly distributed. Exsolved Ni nanoparticles are also found on the surface of the SFNTM substrate particle.

XPS was performed to determine the valence state changes of the surface elements in the as-prepared and reduced SFNTM samples. Figure 3A and Supplementary Table S2 show the Ni 2p spectra of the samples, before and after the reduction treatment. The figure shows a distinct Ni^0 characteristic peak at ~852.2 eV in the Ni@SFNTM sample, further proving that Ni metal particles can be exsolved from the perovskite substrate under a reducing atmosphere. Ni^{2+} peaks are also observed in the spectra, showing that only some Ni metal particles are exsolved from the substrate. Figures 3B,C show the XPS spectra of Fe 2p and Mo 3 d for the Ni@SFNTM and SFNTM samples at room temperature. The peaks at 709.7, 711.3 and 713.0 eV belong to Fe^{2+}, Fe^{3+}, and Fe^{4+}, respectively (Zhang B.-W. et al., 2022). As shown in Supplementary Table S3, both the Fe^{3+} and Fe^{4+} contents decrease and the Fe^{2+} content increases after reduction; the average valence of Fe decreases from 3.00 to 2.79. Moreover,

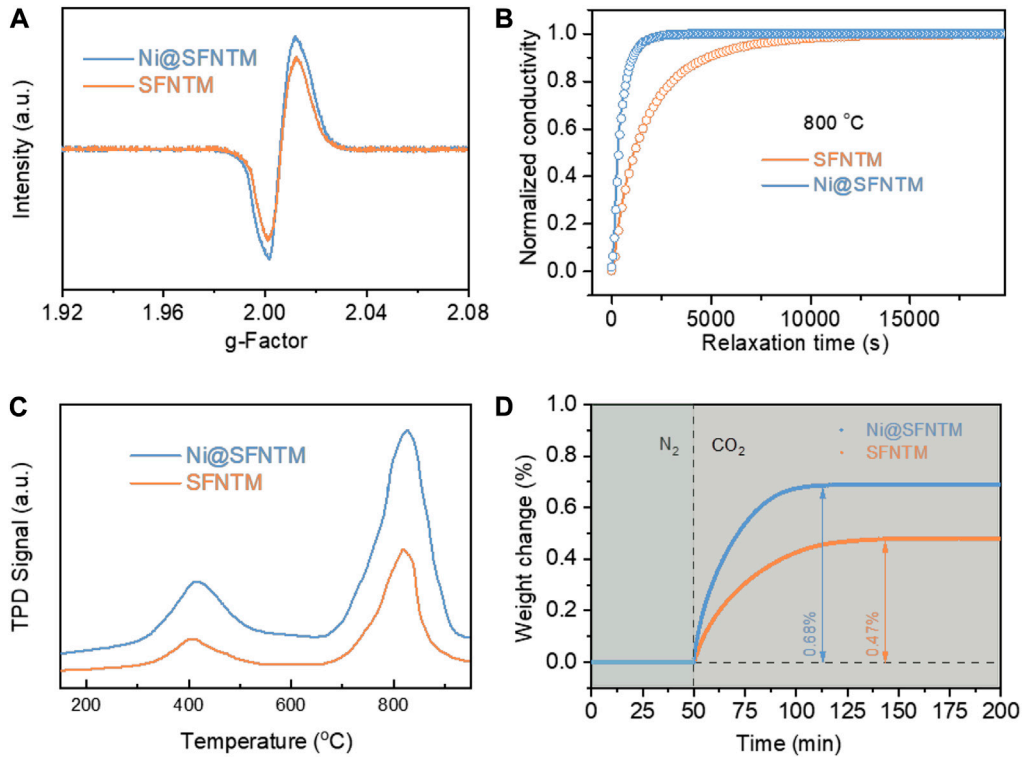

FIGURE 4
(A) EPR measurements and **(B)** ECR curves of SFNTM and Ni@SFNTM samples, **(C)** CO_2-TPD curves at 800°C, tested after abrupt change of the atmosphere from 2:1 CO-CO_2 to 1:1 CO-CO_2, **(D)** Thermogravimetric relaxation curves on changing test gas from N_2 to CO_2 at 600°C.

the Mo 3 d spectrum presents a spin-orbit doublet structure, belonging to a mixed state of Mo^{5+} and Mo^{6+}. It can also be seen in Supplementary Table S4 that the Mo^{6+}/Mo^{5+} ratio decreases after the reduction treatment and the average valence decreases from 5.60 to 5.55, indicating the generation of oxygen vacancies in the SFNTM substrate. The elemental valence states of the Ni, Fe, and Mo transition metals strongly affect the electrocatalytic activity and ionic conductivity of the two samples. The binding energy distributions of the O 1s spectrum are shown in Figure 3D. There are three distinct peaks in the O 1s spectrum corresponding to lattice oxygen (O_{lat}), adsorbed oxygen species (O_{ads}), and hydroxyl or carbonate (OH^-/CO_3^{2-}) on the powder surface (Zhou et al., 2018; Liu et al., 2021). From the fitting results (Supplementary Table S5), it can be seen that the ratio of O_{ads}/O_{lat} increases from 19.5% to 30.5% after reduction, indicating that the oxygen vacancy concentration and the adsorbed oxygen content on the sample surface are enhanced, promoting the electrochemical reaction process at the electrode.

Electron Paramagnetic Resonance (EPR) analysis was used to determine the relative peak intensities of the SFNTM and Ni@SFNTM samples, which correspond to the spin numbers of the lone electrons. Ni@SFNTM shows a higher relative peak intensity than that of SFNTM (Figure 4A), indicating that Ni@SFNTM has a higher concentration of oxygen vacancies; this result is consistent with the XPS results of the O 1s spectra (Figure 3D) (Xi et al., 2021) Moreover, the surface oxygen exchange and bulk diffusion properties of the two samples were evaluated using the ECR method, which can imply the kinetics of the surface CO_2-RR and bulk diffusion in a CO_2-rich atmosphere (Zhu et al., 2016; Li et al., 2019). Figure 4B shows that the oxygen exchange rate can reach equilibrium state with an increase in the CO_2 concentration. The shorter the relaxation time, the faster the oxygen exchange rate. The Ni@SFNTM sample presents a shorter relaxation time than the SFNTM sample at 800°C, implying that the Ni@SFNTM sample has a faster oxygen ion exchange rate due to the increased oxygen vacancies after reduction and can speed up the oxygen transfer process. Additionally, the calculated surface exchange coefficients (K_{chem}) of SFNTM and Ni@SFNTM are 2.42×10^{-5} cm s^{-1} and 8.67×10^{-5} cm s^{-1}, respectively. The corresponding chemical bulk diffusion coefficients (D_{chem}) are 2.58×10^{-6} cm^2 s^{-1} for SFNTM and

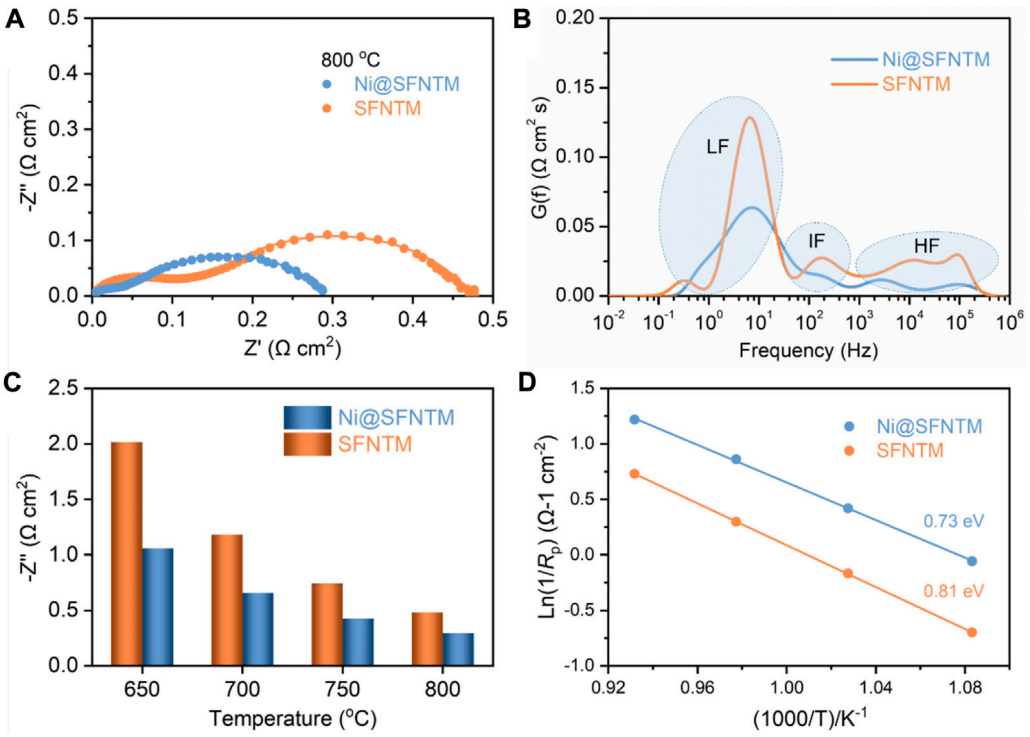

FIGURE 5
(A) EIS patterns of SFNTM and Ni@SFNTM powders at 800°C, and **(B)** corresponding distribution of the relaxation time (DRT) curves, **(C)** Impedance values of two samples from 650 to 800°C, **(D)** CO_2-RR activation energy at 650–800°C.

7.85×10^{-6} cm^2 s^{-1} for Ni@SFNTM. In SOECs, the CO_2 chemisorption process on the surface of the cathode is a rate-limiting step for CO_2-RR, where the adsorption capacity of CO_2 is crucial for the cathode materials of SOEC (Lv et al., 2021). The CO_2 adsorption properties of Ni@SFNTM and SFNTM were determined using CO_2-TPD measurements (Figure 4C). Two desorption peaks at ~400 and ~800°C can be clearly observed in the desorption process of CO_2 corresponding to the physical desorption and the chemical desorption, respectively. At low temperatures, both samples exhibit similar physical desorption processes (Ye et al., 2017). However, both the chemical desorption peak and the corresponding peak area of Ni@SFNTM are higher than those of SFNTM at high temperatures, indicating an enhanced strong binding force for CO_2 adsorption caused by the increased oxygen vacancy and exsolved Ni nano particles. Furthermore, thermogravimetric relaxation was used to investigate the weight changes of the Ni@SFNTM and SFNTM samples by rapidly switching the N_2 atmosphere to a CO_2 atmosphere at 600°C. Figure 4D shows that the weights of the two samples rapidly increase owing to the adsorption of CO_2 and reach equilibrium when the adsorption of CO_2 reached saturation. The Ni@SFNTM sample has a higher weight increase (0.68 %) and shorter adsorption time, indicating that Ni@SFNTM has more oxygen vacancies and stronger CO_2 chemisorption. This result is in good agreement with the XPS and CO_2-TPD results.

In order to study the electrochemical performance and analyze the CO_2 electrolysis reaction of the two cathode materials, EIS was performed on the LSGM electrolyte-supported single cells with the configuration of SFNTM/Ni@SFTNM|SDC|LSGM|LSCF under a pure CO_2 atmosphere at an OCV. Figure 5A shows the polarization resistance (R_p) of a single cell with Ni@SFNTM and SFNTM as cathodes at 800°C. The R_p value of Ni@SFNTM is 0.29 Ω cm^{-2}, which is much lower than that of SFNTM (0.48 Ω cm^{-2}). The EIS data obtained at applied potential of 1.4 V and 800°C were analyzed, as shown in Supplementary Figure S3. Clearly, the SOEC with the Ni@SFNTM cathode significantly reduces the *R*p at 1.4 V, which is consistent with the OCV. Owing to the high catalytic activity of Ni metal and enhanced oxygen vacancies, the reduced R_p improves the CO_2-RR activity of Ni@SFNTM. Figure 5B shows the distribution of the relaxation time (DRT) technology used to explore the separation of the pivotal electrode reaction processes and analyze the deconvolution of the EIS data to further understand the CO_2-RR electrocatalysis process (Zhang et al., 2015; Zhang et al., 2016). There are three areas in the DRT curves of the Ni@SFNTM and SFNTM samples.

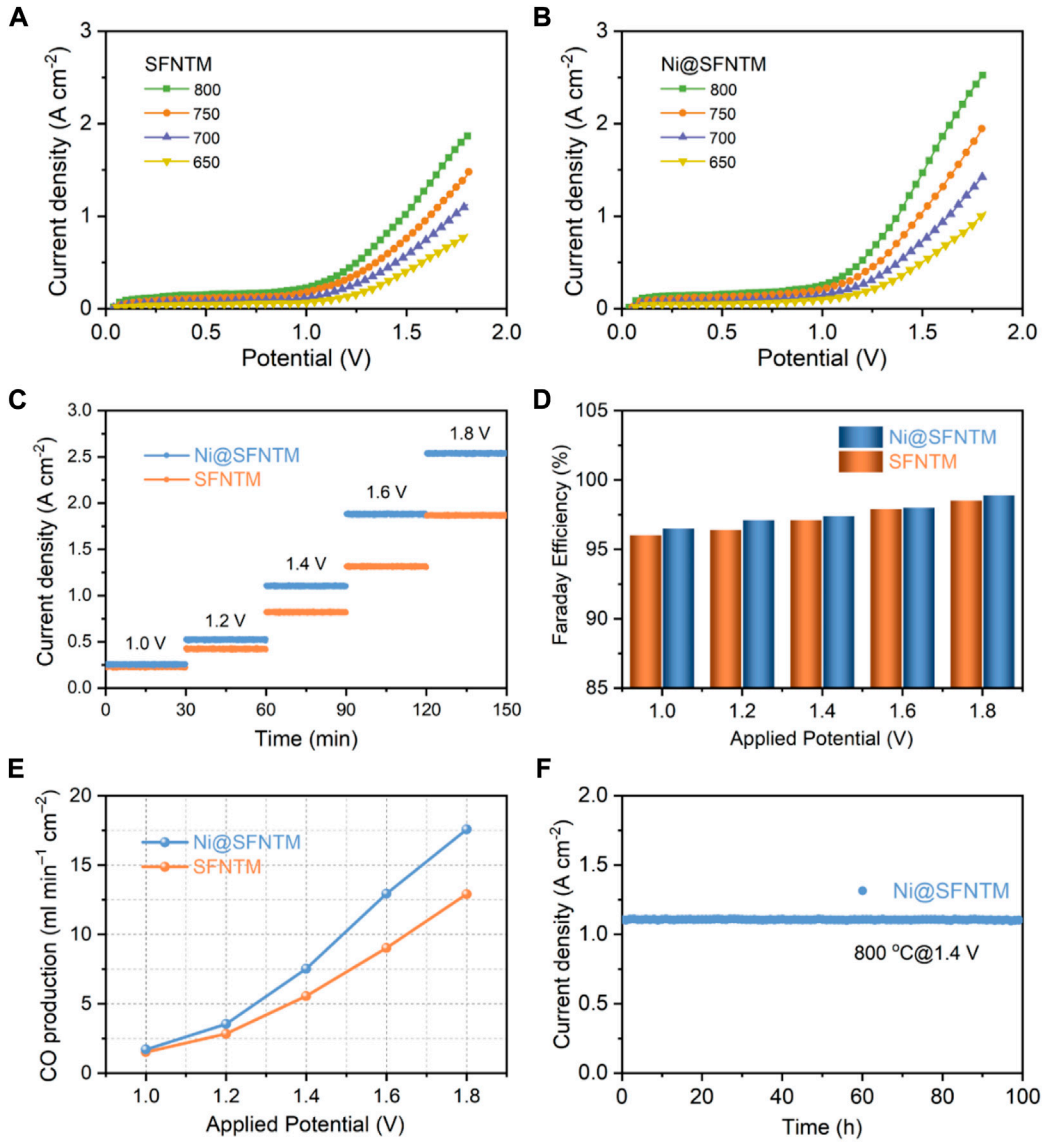

FIGURE 6
Electrochemical performance of **(A)** SFNTM and **(B)** Ni@SFNTM samples under pure CO_2 atmosphere, **(C)** Short-term stability under different applied potentials at 800°C, **(D)** Comparison of Faradaic efficiency under different application potentials, and **(E)** corresponding CO production rate, **(F)** Long-term stability of single cell with Ni@SFNTM cathode under pure CO_2 atmosphere at 1.4 V and 800°C.

The peaks in the high-frequency area (HF) are primarily associated with the oxygen evolution reaction in the anode and the transportation of O^{2-} through the interface of the electrodes and electrolyte (Zhou et al., 2018; Jiang et al., 2019). The low-frequency (LF) area is likely attributed to gas adsorption and the dissociation processes on the cathode surface (Li et al., 2017b). Additionally, the intermediate frequency (IF) is between HF and LF, and represents reactant diffusion and surface processes (Chen et al., 2018; Tian et al., 2020). Both IF and LF exhibit kinetic processes on the electrode surface. It is worth noting that the IF and LF of the Ni@SFNTM cathode significantly decreases, demonstrating that the CO_2 adsorption and electrolysis reaction processes improved. The positions of the characteristic peaks related to IF and LF shift to higher frequencies, suggesting that the electrochemical reaction kinetics should be accelerated. In contrast, after the reduction treatment, the exsolved Ni metal and the increased oxygen vacancies supply more active reaction sites for CO_2 adsorption and activation, while the formed metal-oxide heterostructure with strong interaction enhances the surface exchange reactions (Lee et al., 2021; Zhang L. H. et al., 2022). This occurrence indicates that the CO_2-RR performance of the Ni@SFNTM

cathode is enhanced. These results are in agreement with the XPS, TDP, and ECR results. Moreover, the *R*p values of the two cathodes at different operating temperatures are investigated as shown in Figure 5C. The polarization resistances of both cathodes decrease with an increase in temperature, and the *R*p values of the Ni@SFNTM cathode are lower than those of the SFNTM cathode at a certain temperature. Furthermore, the lower activation energy of the Ni@SFNTM cathode (Figure 5D) also confirms the improved CO_2-RR kinetics and enhanced O^{2-} transportation, primarily resulting from the heterostructure and extended reactive area (Lv et al., 2022).

Consequently, the current-voltage (*I-V*) curves of the single cells with SFNTM and Ni@SFNTM cathodes were measured at 650–800°C respectively, (Figures 6A,B). The CO_2 electrolysis current density of the Ni@SFNTM cathode is 2.54 A cm^{-2} at 1.8 V and 800°C, outperforming the SFNTM cathode (1.86 A cm^{-2}). Because of the anodes and electrolytes of the single cells are similar, the improved CO_2-RR performance can be mainly ascribed to the excellent electrocatalytic activity of the Ni@SFNTM cathode. Moreover, the current densities of Ni@SFNTM are also comparable to those of other perovskite oxide cathodes (Supplementary Table S6). The short-term stability measurements of CO_2-RR at various voltages are shown in Figure 6C; the Ni@SFNTM-based single cell exhibits an excellent CO_2-RR performance at different electrolysis potentials. For instance, the current densities of the single cells with Ni@SFNTM cathode are 1.88 and 2.54 A cm^{-2} at 1.6 and 1.8 V, respectively, which is approximately 1.43 and 1.36 times than that of the single cell with the SFNTM cathode (1.31 and 1.87 A cm^{-2}). Furthermore, gas chromatographic analysis was used to obtain the CO production rate and corresponding Faradaic efficiency by evaluating the exhaust gas collected at different applied potentials during short-time stability measurements. As shown in Figures 6D,E, both the CO production rate and Faradaic efficiency of the two cells increase with increasing applied potential; the Faradaic efficiency of both cells is close to 100%, demonstrating that CO is the primary product and there is no coke deposition during CO_2 electrolysis. The CO generation rate of the Ni@SFNTM-based single cell is 12.5 ml min^{-1} cm^{-2} at 1.6 V, approximately 1.56 times that of the SFNTM-based single cell (8 ml min^{-1} cm^{-2}). This further demonstrates that the formed metal-oxide heterostructure significantly enhances the CO_2-RR performance. Additionally, the single cell with the Ni@SFNTM cathode exhibits excellent long-term operational stability. Figure 6F shows that a stable current density is maintained for 100 h under an applied potential of 1.4 V at 800°C in a pure CO_2 atmosphere. These results indicate that Ni@SFNTM with a Ni metal and SFNTM oxide heterostructure is a potential SOEC cathode for highly efficient CO_2 electrolysis.

Conclusion

In this study, Ti and Ni co-doped SFM perovskite oxides were prepared and used as cathodes for the direct electrolysis of CO_2 in SOECs. A metal-oxide heterostructure was obtained after a reducing treatment in 5% H_2/Ar at 800°C, providing more reactive sites for CO_2-RR, enhancing the chemisorption and activation capacity of CO_2, and significantly improving electrolysis performance. Moreover, the single cell with Ni@SFNTM cathode presented a large CO_2 electrolysis current density of 2.54 A cm^{-2} at 1.8 V and 800°C, exceeding that of the cell comprising the SFNTM cathode (1.87 A cm^{-2} at 1.8 V); it also exhibits excellent long-term stability. This improved performance is primarily attributed to the metal-oxide heterostructure and abundant oxygen vacancies created by the reduction treatment and the strong interaction between the metal and oxide. These results indicate that Ni@SFNTM with the Ni metal and SFNTM oxide heterostructure is a potential SOEC cathode for the efficient electrolysis of CO_2, and this method provides a common strategy for designing high performance electrode materials for SOECs.

Data availability statement

The original contributions presented in the study are included in the article/Supplementary Material, further inquiries can be directed to the corresponding authors.

Author contributions

SZ, main experiment conduct and data curation, manuscript writing. LZ and CX, literature survey, characterization of materials and manuscript curation. DZ and QY, project supervision, financial support, critical review, and manuscript discussion. WS, Data analysis, drawing, manuscript writing and revision. KS, supervision and funding acquisition.

Funding

The work was financially supported by the National Natural Science Foundation of China (Grant Nos 22178023 and 22078022) and Fundamental Research Funds for the Central Universities (FRF-TP-19–077A1).

Acknowledgments

We also thank financial support from the Knowledge Innovation Program of Wuhan -Basic Research (2022020801010354) and Shanxi-Zheda Institute of Advanced Materials and Chemical Engineering (2022SX-TD015).

Conflict of interest

The authors declare that the research was conducted in the absence of any commercial or financial relationships that could be construed as a potential conflict of interest.

Publisher's note

All claims expressed in this article are solely those of the authors and do not necessarily represent those of their affiliated organizations, or those of the publisher, the editors and the reviewers. Any product that may be evaluated in this article, or claim that may be made by its manufacturer, is not guaranteed or endorsed by the publisher.

Supplementary material

The Supplementary Material for this article can be found online at: https://www.frontiersin.org/articles/10.3389/fchem.2022.1027713/full#supplementary-material

References

Armaroli, N., Balzani, V. (2011). The legacy of fossil fuels. *Chem. Asian J.* 6, 768–784. doi:10.1002/asia.201000797

Broecker, W. (2018). CO_2: Earth's climate driver. *Geochem. Perspect.* 7, 117–196. doi:10.7185/geochempersp.7.2

Chen, Y., Yoo, S., Choi, Y., Kim, J. H., Ding, Y., Pei, K., et al. (2018). A highly active, CO_2-tolerant electrode for the oxygen reduction reaction. *Energy Environ. Sci.* 11, 2458–2466. doi:10.1039/c8ee01140k

Choi, J., Park, S., Han, H., Kim, M., Park, M., Han, J., et al. (2021). Highly efficient CO_2 electrolysis to CO on Ruddlesden-Popper perovskite oxide with *in situ* exsolved Fe nanoparticles. *J. Mat. Chem. A Mat.* 9, 8740–8748. doi:10.1039/d0ta11328j

Dong, D. H., Xu, S. S., Shao, X., Hucker, L., Marin, J., Pham, T., et al. (2017). Hierarchically ordered porous Ni-based cathode-supported solid oxide electrolysis cells for stable CO_2 electrolysis without safe gas. *J. Mat. Chem. A Mat.* 5, 24098–24102. doi:10.1039/c7ta06839e

Fu, H. C., You, F., Li, H. R., He, L. N. (2019). CO_2 capture and *in situ* catalytic transformation. *Front. Chem.* 7, 525. doi:10.3389/fchem.2019.00525

Hoegh-Guldberg, O., Jacob, D., Taylor, M., Bolanos, T. G., Bindi, M., Brown, S., et al. (2019). The human imperative of stabilizing global climate change at 1.5°C. *Science* 365, eaaw6974. doi:10.1126/science.aaw6974

Jiang, Y., Yang, Y., Xia, C., Bouwmeester, H. J. (2019). $Sr_2Fe_{1.4}Mn_{0.1}Mo_{0.5}O_{6-\delta}$ perovskite cathode for highly efficient CO_2 electrolysis. *J. Mat. Chem. A Mat.* 7, 22939–22949. doi:10.1039/c9ta07689a

Karanikolos, G. N., Romanos, G. E., Vega, L. F. (2021). Editorial: Chemical modification of adsorbents for enhanced carbon capture performance. *Front. Chem.* 9, 657669. doi:10.3389/fchem.2021.657669

Lee, S., Kim, M., Lee, K. T., Irvine, J. T. S., Shin, T. H. (2021). Enhancing electrochemical CO_2 reduction using $Ce(Mn, Fe)O_2$ with $La(Sr)Cr(Mn)O_3$ cathode for high-temperature solid oxide electrolysis cells. *Adv. Energy Mat.* 11, 2100339. doi:10.1002/aenm.202100339

Li, Y. H., Chen, X. R., Yang, Y., Jiang, Y. N., Xia, C. R. (2017a). Mixed-conductor $Sr_2Fe_{1.5}Mo_{0.5}O_{6-\delta}$ as robust fuel electrode for pure CO_2 reduction in solid oxide electrolysis cell. *ACS Sustain. Chem. Eng.* 5, 11403–11412. doi:10.1021/acssuschemeng.7b02511

Li, Y. H., Hu, B. B., Xia, C. R., Xu, W. Q., Lemmon, J. P., Chen, F. L. (2017b). A novel fuel electrode enabling direct CO_2 electrolysis with excellent and stable cell performance. *J. Mat. Chem. A* 5, 20833–20842. doi:10.1039/c7ta05750d

Li, Y. H., Li, Y., Wan, Y. H., Xie, Y., Zhu, J. F., Pan, H. B., et al. (2019). Perovskite oxyfluoride electrode enabling direct electrolyzing carbon dioxide with excellent electrochemical performances. *Adv. Energy Mat.* 9, 1803156. doi:10.1002/aenm.201803156

Li, Z. S., Cui, L., Luo, J. L., Li, J. H., Sun, Y. F. (2021). Perovskite chromite with *in-situ* assembled Ni-Co nano-alloys: A potential bifunctional electrode catalyst for solid oxide cells. *Front. Chem.* 8, 595608. doi:10.3389/fchem.2020.595608

Liu, C. Y., Li, S. T., Gao, J. Q., Bian, L. Z., Hou, Y. T., Wang, L. J., et al. (2021). Enhancing CO_2 catalytic adsorption on an Fe nanoparticle-decorated $LaSrFeO_{4+\delta}$ cathode for CO_2 electrolysis. *ACS Appl. Mat. Interfaces* 13, 8229–8238. doi:10.1021/acsami.0c18997

Liu, S. B., Liu, Q. X., Luo, J. L. (2016). CO_2-to-CO conversion on layered perovskite with *in situ* exsolved Co-Fe alloy nanoparticles: An active and stable cathode for solid oxide electrolysis cells. *J. Mat. Chem. A Mat.* 4, 17521–17528. doi:10.1039/c6ta06365a

Liu, S., Liu, Q., Luo, J. (2016). Highly stable and efficient catalyst with *in situ* exsolved Fe-Ni alloy nanospheres socketed on an oxygen deficient perovskite for direct CO_2 electrolysis. *ACS Catal.* 6, 6219–6228. doi:10.1021/acscatal.6b01555

Lv, H. F., Lin, L., Zhang, X. M., Gao, D. F., Song, Y. F., Zhou, Y. J., et al. (2019). *In situ* exsolved $FeNi_3$ nanoparticles on nickel doped $_{Sr2Fe1.5Mo0.5O6}$ perovskite for efficient electrochemical CO_2 reduction reaction. *J. Mat. Chem. A Mat.* 7, 11967–11975. doi:10.1039/c9ta03065d

Lv, H. F., Lin, L., Zhang, X. M., Li, R. T., Song, Y. F., Matsumoto, H., et al. (2021). Promoting exsolution of RuFe alloy nanoparticles on $Sr_2Fe_{1.4}Ru_{0.1}Mo_{0.5}O_{6-\delta}$ via repeated redox manipulations for CO_2 electrolysis. *Nat. Commun.* 12, 5665. doi:10.1038/s41467-021-26001-8

Lv, J. W., Sun, W., Xu, C. M., Yang, X. X., Ma, M. J., Zhang, L. H., et al. (2022). Enhancing the catalytic activity and CO_2 chemisorption ability of the perovskite cathode for soild oxide electrolysis cell through *in situ* Fe-Sn alloy nanoparticles. *Sep. Purif. Technol.* 294, 121127. doi:10.1016/j.seppur.2022.121127

Park, S., Kim, Y., Han, H., Chung, Y. S., Yoon, W., Choi, J., et al. (2019). *In situ* exsolved Co nanoparticles on Ruddlesden-Popper material as highly active catalyst for CO_2 electrolysis to CO. *Appl. Catal. B Environ.* 248, 147–156. doi:10.1016/j.apcatb.2019.02.013

Park, S., Kim, Y., Noh, Y., Kim, T., Han, H., Yoon, W., et al. (2020). A sulfur-tolerant cathode catalyst fabricated with *in situ* exsolved CoNi alloy nanoparticles anchored on a Ruddlesden-Popper support for CO_2 electrolysis. *J. Mat. Chem. A Mat.* 8, 138–148. doi:10.1039/c9ta07700f

Quadrelli, E. A., Centi, G., Duplan, J. L., Perathoner, S. (2011). Carbon dioxide recycling: Emerging large-scale technologies with industrial potential. *Chemsuschem* 4, 1194–1215. doi:10.1002/cssc.201100473

Sciazko, A., Shimura, T., Komatsu, Y., Shikazono, N. (2021). Ni-GDC and Ni-YSZ electrodes operated in solid oxide electrolysis and fuel cell modes. *J. Therm. Sci. Technol.* 16, JTST0013. doi:10.1299/jtst.2021jtst0013

Singh, V., Muroyama, H., Matsui, T., Hashigami, S., Inagaki, T., Eguchi, K. (2015). Feasibility of alternative electrode materials for high temperature CO_2 reduction on solid oxide electrolysis cell. *J. Power Sources* 293, 642–648. doi:10.1016/j.jpowsour.2015.05.088

Song, Y. F., Zhou, Z. W., Zhang, X. M., Zhou, Y. J., Gong, H. M., Lv, H. F., et al. (2018). Pure CO_2 electrolysis over an Ni/ YSZ cathode in a solid oxide electrolysis cell. *J. Mat. Chem. A Mat.* 6, 13661–13667. doi:10.1039/c8ta02858c

Tian, Y. F., Liu, Y., Naden, A., Jia, L. C., Xu, M., Cui, W., et al. (2020). Boosting CO_2 electrolysis performance via calcium-oxide-looping combined with *in situ* exsolved Ni-Fe nanoparticles in a symmetrical solid oxide electrolysis cell. *J. Mat. Chem. A Mat.* 8, 14895–14899. doi:10.1039/d0ta05518b

Wang, W. Y., Gan, L. Z., Lemmon, J. P., Chen, F. L., Irvine, J. T. S., Xie, K. (2019). Enhanced carbon dioxide electrolysis at redox manipulated interfaces. *Nat. Commun.* 10, 1550. doi:10.1038/s41467-019-09568-1

Wang, Y., Liu, T., Li, M., Xia, C., Zhou, B., Chen, F. (2016). Exsolved Fe-Ni nanoparticles from $Sr_2Fe_{1.3}Ni_{0.2}Mo_{0.5}O_6$ perovskite oxide as a cathode for solid oxide steam electrolysis cells. *J. Mat. Chem. A Mat.* 4, 14163–14169. doi:10.1039/c6ta06078a

Xi, X. A., Liu, J. W., Luo, W. Z., Fan, Y., Zhang, J. J., Luo, J. L., et al. (2021). Unraveling the enhanced kinetics of $Sr_2Fe_{1+x}Mo_{1-x}O_{6-\delta}$ electrocatalysts for high-performance solid oxide cells. *Adv. Energy Mater.* 11, 2102845. doi:10.1002/aenm.202102845

Xu, C. M., Sun, W., Ren, R. Z., Yang, X. X., Ma, M. J., Qiao, J. S., et al. (2021). A highly active and carbon-tolerant anode decorated with *in situ* grown cobalt nano-catalyst for intermediate-temperature solid oxide fuel cells. *Appl. Catal. B-Environmental* 282, 119553. doi:10.1016/j.apcatb.2020.119553

Xu, C. M., Zhang, L. H., Sun, W., Ren, R. Z., Yang, X. X., Ma, M. J., et al. (2022). Co-improving the electrocatalytic performance and H2S tolerance of a $Sr_2Fe_{1.5}Mo_{0.5}O_{6-\delta}$ based anode for solid oxide fuel cells. *J. Mat. Chem. A Mat.* 10, 16280–16289. doi:10.1039/d2ta03136a

Xu, C. M., Zhen, S. Y., Ren, R. Z., Chen, H. S., Song, W. L., Wang, Z. H., et al. (2019). Cu-Doped $Sr_2Fe_{1.5}Mo_{0.5}O_{6-\delta}$ as a highly active cathode for solid oxide electrolytic cells. *Chem. Commun.* 55, 8009–8012. doi:10.1039/c9cc03455b

Yang, C. C., Tian, Y. F., Pu, J., Chi, B. (2022). Anion fluorine-doped $La_{0.6}Sr_{0.4}Fe_{0.8}Ni_{0.2}O_3$ perovskite cathodes with enhanced electrocatalytic activity for solid oxide electrolysis cell direct CO_2 electrolysis. *ACS Sustain. Chem. Eng.* 10, 1047–1058. doi:10.1021/acssuschemeng.1c07576

Ye, L. T., Zhang, M. Y., Huang, P., Guo, G. C., Hong, M. C., Li, C. S., et al. (2017). Enhancing CO_2 electrolysis through synergistic control of non-stoichiometry and doping to tune cathode surface structures. *Nat. Commun.* 8, 14785. doi:10.1038/ncomms14785

Zhang, B.-W., Zhu, M.-N., Gao, M.-R., Xi, X., Duan, N., Chen, Z., et al. (2022). Boosting the stability of perovskites with exsolved nanoparticles by B-site supplement mechanism. *Nat. Commun.* 13, 4618. doi:10.1038/s41467-022-32393-y

Zhang, L. H., Xu, C. M., Sun, W., Ren, R. Z., Yang, X. X., Luo, Y. Z., et al. (2022). Constructing perovskite/alkaline-earth metal composite heterostructure by infiltration to revitalize CO_2 electrolysis. *Sep. Purif. Technol.* 298, 121475. doi:10.1016/j.seppur.2022.121475

Zhang, S. W., Zhu, K., Hu, X.y., Peng, R. R., Xia, C. R. (2021). Antimony doping to greatly enhance the electrocatalytic performance of Sr2Fe1.5Mo0.5O6-δ perovskite as a ceramic anode for solid oxide fuel cells. *J. Mater. Chem. A.* 9, 24336–24347. doi:10.1039/d1ta06196h

Zhang, X. M., Liu, L., Zhao, Z., Tu, B. F., Ou, D. R., Cui, D. A., et al. (2015). Enhanced oxygen reduction activity and solid oxide fuel cell performance with a nanoparticles-loaded cathode. *Nano Lett.* 15, 1703–1709. doi:10.1021/nl5043566

Zhang, X. M., Wu, W. M., Zhao, Z., Tu, B. F., Ou, D. R., Cui, D. A., et al. (2016). Insight into the oxygen reduction reaction on the LSM|GDC interface of solid oxide fuel cells through impedance spectroscopy analysis. *Catal. Sci. Technol.* 6, 4945–4952. doi:10.1039/c5cy02232k

Zhang, Y. Q., Jacobs, G., Sparks, D. E., Dry, M. E., Davis, B. H. (2002). CO and CO_2 hydrogenation study on supported cobalt Fischer-Tropsch synthesis catalysts. *Catal. Today* 71, 411–418. doi:10.1016/s0920-5861(01)00468-0

Zheng, Y., Wang, J. C., Yu, B., Zhang, W. Q., Chen, J., Qiao, J. L., et al. (2017). A review of high temperature co-electrolysis of H_2O and CO_2 to produce sustainable fuels using solid oxide electrolysis cells (SOECs): Advanced materials and technology. *Chem. Soc. Rev.* 46, 1427–1463. doi:10.1039/c6cs00403b

Zhou, Y. J., Zhou, Z. W., Song, Y. F., Zhang, X. M., Guan, F., Lv, H. F., et al. (2018). Enhancing CO_2 electrolysis performance with vanadium-doped perovskite cathode in solid oxide electrolysis cell. *Nano Energy* 50, 43–51. doi:10.1016/j.nanoen.2018.04.054

Zhu, J. W., Liu, G. P., Liu, Z. K., Chu, Z. Y., Jin, W. Q., Xu, N. P. (2016). Unprecedented perovskite oxyfluoride membranes with high-efficiency oxygen ion transport paths for low-temperature oxygen permeation. *Adv. Mat.* 28, 3511–3515. doi:10.1002/adma.201505959